ACS SENSORS

Article

Cite This: ACS Sens. 2018, 3, 458–467

pubs.acs.org/acssensors

Chromis-1, a Ratiometric Fluorescent Probe Optimized for Two-Photon Microscopy Reveals Dynamic Changes in Labile Zn(II) in Differentiating Oligodendrocytes

Daisy Bourassa,[§,‡] Christopher M. Elitt,[†,‡] Adam M. McCallum,[§] S. Sumalekshmy,[§] Reagan L. McRae,[§] M. Thomas Morgan,[§] Nisan Siegel,[§] Joseph W. Perry,*[,§] Paul A. Rosenberg,*[,†] and Christoph J. Fahrni*[,§]

[§]School of Chemistry and Biochemistry and Petit Institute for Bioengineering and Bioscience, Georgia Institute of Technology, Atlanta, Georgia 30332, United States

[†]Department of Neurology and Program in Neuroscience, Children's Hospital and Harvard Medical School, Boston, Massachusetts 02115, United States

Supporting Information

ABSTRACT: Despite the significant advantages of two-photon excitation microscopy (TPEM) over traditional confocal fluorescence microscopy in live-cell imaging applications, including reduced phototoxicity and photobleaching, increased depth penetration, and minimized autofluorescence, only a few metal ion-selective fluorescent probes have been designed and optimized specifically for this technique. Building upon a donor–acceptor fluorophore architecture, we developed a membrane-permeant, Zn(II)-selective fluorescent probe, chromis-1, that exhibits a balanced two-photon cross section between its free and Zn(II)-bound form and responds with a large spectral shift suitable for emission-ratiometric imaging. With a K_d of 1.5 nM and wide dynamic range, the probe is well suited for visualizing temporal changes in buffered Zn(II) levels in live cells as demonstrated with mouse fibroblast cell cultures. Moreover, given the importance of zinc in the physiology and pathophysiology of the brain, we employed chromis-1 to monitor cytoplasmic concentrations of labile Zn(II) in oligodendrocytes, an important cellular constituent of the brain, at different stages of development in cell culture. These studies revealed a decrease in probe saturation upon differentiation to mature oligodendrocytes, implying significant changes to cellular zinc homeostasis during maturation with an overall reduction in cellular zinc availability. Optimized for TPEM, chromis-1 is especially well-suited for exploring the role of labile zinc pools in live cells under a broad range of physiological and pathological conditions.

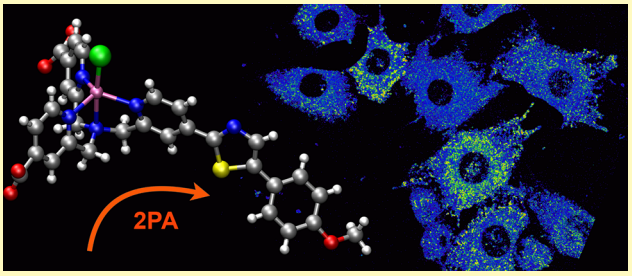

KEYWORDS: *fluorescent probe, two-photon excitation microscopy, zinc homeostasis, live cell imaging, neuroscience*

Fluorescence microscopy ranks among the most widely utilized methods for the noninvasive observation of biological processes in live cells, tissues, and whole organisms. As most biological targets are nonfluorescent, this technique relies on the application of selective fluorescent labels and indicators;[1] however, photobleaching and phototoxicity associated with most fluorophores impose significant limitations, especially for prolonged imaging studies with live specimens. Two-photon excitation microscopy (TPEM), which is based on the simultaneous absorption of two photons with half the energy compared to traditional fluorescence imaging, overcomes many of these challenges with the added benefit of intrinsic 3D imaging capabilities, increased depth penetration, and reduced cellular background fluorescence.[2,3] Although common fluorescent tags can be employed for TPEM imaging, their brightness may be hampered due to low two-photon absorption (2PA) cross sections.[4] The need for TPEM-optimized fluorophores is particularly evident in the area of metal-ion sensing with ratiometric indicators that rely on a chromatic shift for analyte detection.[5,6] Although tunable to a specific wavelength, Ti-sapphire femtosecond-pulsed lasers employed in commercial TPEM instruments cannot alternate between different excitation energies in rapid succession. Therefore, ratiometric TPEM imaging requires indicators that offer not only sufficient brightness, but also respond with a spectral shift of the emission profile,[7] requirements that are currently not met by most ratiometric indicators.[8]

To address these challenges, we employed a fluorophore design strategy that yields both a large 2PA cross section, as well as a chromatic shift in the fluorescence emission upon metal binding.[9] By electronically coupling the analyte binding site to

Received: November 28, 2017
Accepted: January 26, 2018
Published: February 12, 2018

DOI: 10.1021/acssensors.7b00887
ACS Sens. 2018, 3, 458–467

the acceptor moiety of a push−pull fluorophore architecture rather than the donor moiety, coordination of the metal cation elicits an increased intramolecular charge transfer (ICT) upon photoexcitation, which in turn results in a more favorable 2PA cross section along with a red-shifted fluorescence emission. Building upon this approach, we present here a Zn(II)-selective indicator, chromis-1, that features a balanced 2PA cross section between the free and bound probe, combined with a large emission shift suitable for emission-ratiometric TPEM imaging.

In addition to rigorous characterization of the coordination chemistry and photophysical properties, we employed chromis-1 for monitoring dynamic changes of labile Zn(II) pools in live mouse fibroblasts and for assessing differences in the zinc availability in oligodendrocytes at different stages of development. These cells play a critical role in the central nervous system for insulating axons through the formation of a myelin sheath composed of lipids and proteins.[10] As an essential trace element, zinc serves a diverse set of physiological functions in the brain. Cellular zinc pools are tightly controlled by a complex interplay between zinc transporters, influx and efflux pathways, as well as subcellular zinc storage sites.[11,12] Not surprisingly, zinc excess can have profound effects on the developing and mature nervous system. For example, excess zinc released from glutamatergic synapses is a cause of neuronal death during ischemia,[13] and accumulation of zinc following optic nerve injury triggers retinal ganglion cell death.[14] Similarly, surges in intracellular zinc have also been implicated in excitotoxic or nitrative insults to mature oligodendrocytes.[15−17] Despite the demonstrated importance of zinc in the central nervous system, studying homeostatic fluctuations in labile zinc pools that are estimated to be buffered in the picomolar range[18] has been challenging due to a lack of suitable reagents to visualize and probe cellular zinc levels. Optimized for TPEM, chromis-1 addresses this need and should be well-suited for exploring the physiological role of labile zinc pools in the central nervous system.

EXPERIMENTAL SECTION

Synthesis of Chromis-1. Synthetic procedures for compounds **1a**−**b** and all intermediates are provided in the Supporting Information.

X-ray Structure Determination. Single colorless plate-shaped crystals of the Zn(II)-complex of chromis-1 acid **1b** were grown as described in the Supporting Information. A suitable crystal (0.19 × 0.10 × 0.03 mm^3) was selected and mounted on a loop with paratone oil on a Bruker APEX-II CCD diffractometer. The crystal was cooled to T = 100(2) K during data collection. The structure was solved with the ShelXT-2014/4[19] structure solution program using combined Patterson and dual-space recycling methods and by using Olex2[20] as the graphical interface. The crystal structure was refined with version 2014/7 of ShelXL[21] using Least Squares minimization. Crystal structure data and structure refinement parameters are provided in Table S1 of the Supporting Information.

Liposome Preparation. A solution of 32.3 mg 1,2-dimyristoyl-*sn*-glycero-3-phosphocholine (DMPC) and 8.2 mg 1,2-dimyristoyl-*sn*-glycero-3-phospho-(1′-rac-glycerol) (DMPG) in 4:1 dichloromethane-methanol (20 mL) was evaporated under reduced pressure followed by drying for 2 h in high vacuum. The resulting film was hydrated with aqueous buffer (29.8 mL, 20 mM PIPES, 0.1 M KCl, pH 7.0), sonicated for 5 min, and left to equilibrate for 5 h. After dilution to a concentration of 500 μM, the hydrated lipids were passed 21 times through an extruder (Liposofast, Avestin) using a polycarbonate membrane with 200 nm pore size. Liposome particle sizes were determined based upon the Tunable Resistance Pulse Sensing (TRPS) principle using the Izon qNano particle analyzer (Izon Science, Ltd., Burnside, New Zealand) to afford an average diameter of 122 nm.[22] Freshly extruded lipids were used immediately.

Photophysical Characterization. All buffers and stock solutions were prepared with 18.2 MΩ·cm Milli-Q water and filtered through 0.2 μm membrane filters to remove interfering particles or fibers. UV−vis absorption measurements were acquired at 25 °C using a Cary Bio50 spectrophotometer (Varian) with constant temperature accessory. Fluorescence measurements were performed with a PTI fluorimeter equipped with a 75 W xenon arc lamp excitation source and a photomutiplier detection system. Fluorescence spectra were corrected for the spectral response of the detection system and the spectral irradiance of the excitation source (via a calibrated photodiode). Spectra were acquired using quartz cuvettes with 10 cm path length for the OD measurements of quantum yield determinations and 1 cm path length for all other measurements.

Fluorescence quantum yields were determined using quinine sulfate as a reference (Φ_f = 0.55 in 1.0 N H_2SO_4)[23] with excitation at 365 nm by a 4-point measurement over an OD range of 0.1−0.4 (l = 10 cm) in pH 7.0 buffer (10 mM PIPES, 0.1 M KCl, 25 °C). In the case of lipophilic chromis-1 ester (**1a**), measurements were performed by diluting the compound from a 3 mM DMSO stock solution to a final concentration of 2 μM in pH 7.0 buffer containing 100 μM 4:1 DMPC:DMPG liposomes.[22] To sequester adventitious Zn(II), quantum yields of free chromis-1 ester and acid were determined in the presence of 20 μM EDTA.

Metal Ion Selectivity. A 5 μM solution of chromis-1 acid **1b** was prepared in pH 7.0 buffer (10 mM PIPES, 0.1 M KCl), which had been treated with Chelex (1% w/v, Biorad) overnight. Metal ions were supplied from aqueous stock solutions (1 M for Mg(II) and Ca(II), 1 mM for all other metal ions) of the corresponding sulfate salts (Mn(II), Fe(II), Cu(II), and Zn(II)) or nitrate salts (Mg(II), Ca(II), Co(II), and Ni(II)). Fluorescence spectra were acquired in the absence and upon addition of 0.8 mol equiv of the respective metal ions (excitation at 358 nm). Responses to Mg(II) and Ca(II) were measured each at a concentration of 2 mM. In addition, fluorescence spectra were acquired after saturating the remaining 0.2 mol equiv of the probe by supplementation with 1 μM Zn(II). All ratios R = BP2/BP1 were calculated based on the integrated fluorescence between 510 and 570 nm (BP2) and 440 and 495 nm (BP1).

Stability Constants. Chromis-1 acid **1b** (20 μM) in pH 7.0 buffer (10 mM PIPES, 0.1 M KCl, pH 7.0, 25 °C) was saturated with 1.0 molar eq of Zn(II) supplied from a 6 mM stock solution of $ZnSO_4 \cdot 7H_2O$ in deionized H_2O and then titrated with EGTA up to a total concentration of 0.5 mM. After addition of each aliquot, the solution was equilibrated for 10 min and a UV−vis spectrum was acquired over the range of 250−500 nm. The spectral data were analyzed by nonlinear least-squares fitting using SPECFIT.[24] to yield an average apparent log$K$ of 10.31 ± 0.13 (Figure S2).

To determine the Zn(II) stability constant of chromis-1 ester **1a**, the compound was diluted from a 3 mM DMSO stock solution to a final concentration of 2 μM in pH 7.0 buffer (20 mM PIPES, 0.1 M KCl, pH 7.0, 25 °C) containing 1.0 mM EGTA and 100 μM liposomes (4:1 mixture of DMPC and DMPG, vide infra). The solution (3.0 mL total volume) was equilibrated at 25 °C with gentle stirring for a minimum of 10 min, and then titrated with Zn(II) to a final concentration of 1 mM. After addition of each aliquot of Zn(II), the solution was equilibrated for 5 min, and a fluorescence spectrum was acquired over the spectral window of 380−680 nm with excitation at 358 nm (Figure S3). The data were analyzed by nonlinear least-squares fitting over the entire spectral range using SPECFIT.

Protonation Constants. A combination glass electrode with double junction was calibrated based on Gran's method by titrating a 5 mM solution of HCl in 0.1 M KCl with a standardized solution of 0.1 M KOH at 25 °C. The titration data were analyzed with the GLEE software package to derive the corresponding electrode potential $E°$ and slope s relating the measured emf with the hydronium ion concentration p[H] or −log[H_3O^+].[25] The sequential protonation constants of chromis-1 acid **1b** were determined based on spectrophotometric titrations at 25 °C. To this end, a solution of **1b** (22.7 μM) was prepared in a mixed buffer (1 mM PIPES/PIPBS, 0.1 M KCl, pH 7.1) and a total of 50 UV−vis spectra were acquired in a quartz cuvette (1 cm path length) over a p[H] range from 7.1 to 1.0. The titration solution was gradually acidified

DOI: 10.1021/acssensors.7b00887
ACS Sens. 2018, 3, 458−467

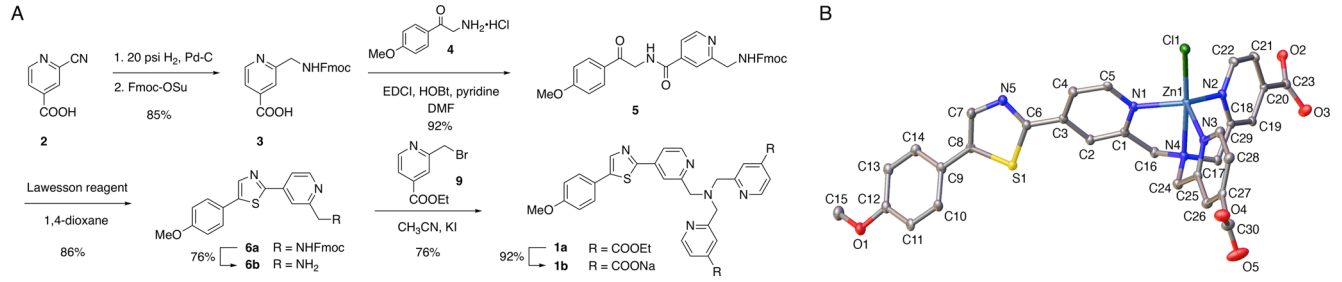

Figure 1. (A) Synthetic scheme for the assembly of chromis-1 (**1**). (B) ORTEP representation and atom numbering scheme for the crystal structure of the Zn(II)-complex of chromis-1 acid **1b**. Ellipsoids shown represent 50% probability. Hydrogen atoms and counterions have been omitted for clarity. Detailed crystallographic data are provided in the Supporting Information (Table S1–S3).

by addition of 1–10 μL aliquots of aqueous HCl supplied from 0.1, 1, or 6 M stock solutions. The combined UV–vis traces were analyzed by nonlinear least-squares fitting over the entire spectral range (300–500 nm) using the SPECFIT software package.[24] Titration data, deconvoluted spectra for each protonation state, and a species distribution diagram are provided in the Supporting Information (Figure S5).

pH-Dependent Response. Two batches of 2 mM 4:1 DMPC:DMPG liposomes were prepared according to the procedure described above in pH 5.0 buffer (10 mL of 10 mM PIPES, 0.1 M KCl) and pH 7.0 buffer (10 mL of 10 mM PIPES, 0.1 M KCl), respectively. Freshly extruded liposomes were diluted to 100 μM final concentration in the respective buffer solutions and equilibrated in a quartz cuvette for 15 min at 25 °C. Chromis-1 ester was added from a 3 mM DMSO stock solution to a final concentration of 2 μM. After an additional 10 min equilibration period, a fluorescence spectrum was acquired from 380 to 700 nm with excitation at 358 nm. Spectra of the Zn(II)-saturated probe at pH 5 and 7 were acquired after addition of an equimolar amount of $ZnSO_4 \cdot 7H_2O$ supplied from a 3 mM stock solution in water (Figure S4).

Cell Culture and Reagents. NIH 3T3 mouse fibroblasts were cultured in Dulbecco's modified Eagle's medium (DMEM, Lonza) supplemented with 10% bovine serum (Gemini), penicillin/streptomycin (50 IU/mL), 200 μM L-glutamine, and 100 μM sodium pyruvate at 37 °C under an atmosphere of humidified air containing 5% CO_2.

For oligodendrocyte cultures, mixed glia cultures were first prepared from post-natal day 2 (P2) rat forebrains and grown for 10–17 days as previously described.[26] In brief, developing OLs were separated from microglia and astrocytes using selective detachment and then plated onto coverslips. Cells were maintained in the presence of platelet-derived growth factor (PDGF) and basic fibroblast growth factor (FGF) for 8 days prior to imaging. To produce mature OLs, PDGF and FGF were replaced by triiodothyronine (T3) and ciliary neurotrophic factor (CNTF) and cultured for an additional week. Media was changed every other day with 2× growth factors. Health of the cells was determined by visual inspection using phase contrast microscopy.

Two-Photon Microscopy. For imaging experiments, cells were grown to 70% confluency on MatTek glass bottom culture dishes precoated with poly(L-lysine) using phenol red-free DMEM (10% bovine serum, 50 IU/mL penicillin/streptomycin, 200 μM L-glutamine, and 100 μM sodium pyruvate). After replacing the growth medium with serum-free DMEM containing chromis-1 ester (10 μM), cells were incubated for 15 min at 37 °C (5% CO_2 atmosphere), and the incubation solution was again replaced with prewarmed full media. Cells were imaged in an atmospheric chamber at 37 °C, 8% humidity, and 5% CO_2 using a Zeiss LSM confocal NLO 710 microscope equipped with a femtosecond pulsed Ti:sapphire laser. Scanning fluorescence micrographs were acquired with excitation at 720 nm, and the integrated emission intensity was simultaneously collected through two band-pass filters between 425 and 462 nm and 478 and 540 nm. Reagents for probing the response of chromis-1, including pyrithione, $ZnSO_4$, *N*,*N*,*N*′,*N*′-tetrakis(2-pyridylmethyl)ethylenediamine (TPEN), 2,2′-dithiodipyridine (DTDP), and bafilomycin A_1 were directly added from DMSO stock solutions to the dish mounted on the microscope stage. Ratiometric image analysis was performed with ImageJ[27] as outlined in the Supporting Information.

For colocalization with cellular marker proteins, cells were grown to 30–40% confluency on MatTek glass bottom dishes as described above and transfected with 2 μg of either pDsRed2-mito or pEYFP-ER plasmids using Turbofect (4 μL in 200 μL DMEM, Thermo Scientific). After 24 h, the growth medium was replaced with serum-free medium containing chromis-1 ester. Cells were incubated for 15 min, and the medium was replaced with prewarmed full media for acquiring fluorescence micrographs as described above. Fluorescence emission of both chromis-1 and the respective fluorescent organelle markers were collected simultaneously with the laser and filter settings switching on a line-by-line basis while scanning (chromis-1 ester: λ_{ex} 720 nm, λ_{em} BP 400–498 nm, DsRed2-mito: λ_{ex} 562 nm, λ_{em} BP 570–700 nm, EYFP-ER: λ_{ex} 514 nm, λ_{em} BP 525–700 nm). For colocalization with lipid droplets, cells were costained with 10 μM chromis-1 ester and 2 μM BODIPY 493/503 (4,4-difluoro-1,3,5,7,8-pentamethyl-4-bora-3*a*,4*a*-diaza-*s*-indacene, Thermo Fisher, λ_{ex} 488 nm, λ_{em} BP 525–675 nm), or 50 nM LysoTracker Red (Thermo Fisher, λ_{ex} = 514 nm, λ_{em} 525–675 nm).

Chromis-1 Imaging and Analysis with Oligodendrocytes. On the day of imaging, media containing chromis-1 ester (10 μM) was added without growth factors and incubated at 37 °C for 30 min. Medium containing chromis-1 was removed, cells were washed with Hanks Buffered Saline Solution (HBSS) containing calcium and magnesium and then transferred to 60 mm dishes containing HBSS. Imaging was performed using a Zeiss LSM710 confocal microscope equipped for 2-photon microscopy. Zinc-pyrithione and TPEN were pipetted onto the coverslips using concentrated stock solutions. Ratiometric image analysis was performed in ImageJ as above. Statistical differences were calculated using prism software.

RESULTS AND DISCUSSION

Synthesis. Following a convergent synthetic approach, chromis-1 was assembled from three building blocks, the Fmoc-protected amino acid **3**, α-amino ketone **4**, and pyridine derivative **9** (Figure 1A). While the latter two were synthesized based on modified literature procedures,[9,28] acid **3** was accessible in two steps from inexpensive isonicotinic acid *N*-oxide. Alkylation with dimethylsulfate followed by vicarious nucleophilic substitution with NaCN yielded 2-cyanoisonicotinic acid **2**, which was converted to Fmoc-protected **3** in a one-pot procedure with 85% overall yield. The bridging thiazole unit of the fluorophore π-system was constructed by EDCI-mediated condensation of **3** and **4** followed by thionation-cyclization of coupling intermediate **5** with Lawesson's reagent. Subsequent Fmoc-deprotection yielded intermediate **6b** with 65% overall yield. By using ethanethiolate as the base in lieu of piperidine that is commonly employed for Fmoc-removal, amine **6b** could be isolated in analytically pure form through simple acid–base extraction. Similarly, intermediates **5** and **6a** were isolated and crystallized in high yield without the need for chromatographic

DOI: 10.1021/acssensors.7b00887
ACS Sens. 2018, 3, 458–467

purification. The synthesis was concluded by nucleophilic substitution of amine **6b** with **9** to afford crystalline chromis-1 ester **1a**, a portion of which was hydrolyzed to give chromis-1 acid **1b** as the corresponding water-soluble disodium salt.

X-ray Structure Determination. The Zn(II) complex of chromis-1 acid was crystallized from a mixture of aqueous KCl (0.1 M), DMF, and MeOH to produce plate-like single crystals suitable for X-ray crystallographic analysis. The unit cell of the triclinic crystals contained two conformers with notable structural differences. A list of selected bond angles and distances is provided in the Supporting Information (Table S2, Supporting Information). As illustrated in Figure 1B for one of the two conformers, the Zn(II)-complex adopts a trigonal-bipyramidal coordination geometry with chloride in the axial position. Compared to previously published structures of the unsubstituted C3-symmetric [tris(picolyl)amine-Zn(II)Cl]$^+$ complex,[29−31] the equatorial Zn−N bonds are elongated by an average of 0.03 ± 0.01 Å. The slightly weaker interaction with the pyridine ligands can be attributed to the electron-withdrawing character of the thiazole and carboxylic acid substituents. In contrast, there are no significant differences for the axial Zn−Cl and Zn−N bonds, which adopt in all structures a uniform bond length of 2.26 ± 0.01 Å. In both conformers, the fluorophore architecture exhibits some deviation from planarity as evident from the dihedral angles of the corresponding aryl−aryl bonds. The largest difference is observed for the anisole ring, which is rotated out of plane by 35° relative to the thiazole, however, in only one of the two conformers. The near-planar dihedral angle of 14.7° for the second conformer suggests that the distortion is associated with a soft potential and likely due to packing forces.

Steady-State Absorption and Fluorescence Properties. Molar ratio titrations of chromis-1 acid (**1b**) with Zn(II) in neutral aqueous buffer (pH 7.0, 10 mM PIPES 0.1 M KCl, 25 °C) revealed strong chromatic shifts in both the absorption and emission spectra together with sharp saturation at equimolar metal and ligand concentrations (Figure 2A and B). Pertinent photophysical data, including quantum yields, are compiled in Table 1. Consistent with Zn(II)-coordination to the pyridyl acceptor moiety of the fluorophore, the absorption maximum at 349 nm ($\varepsilon \sim 20{,}500\ M^{-1}\ cm^{-1}$) is red-shifted by 17 nm upon saturation with Zn(II). The appearance of clean isosbestic points at 285 and 353 nm combined with equimolar saturation are indicative of a well-defined solution equilibrium involving only free probe and a Zn(II)-complex with 1:1 metal−ligand stoichiometry. Similarly, the fluorescence emission maximum of the probe is red-shifted from 483 to 520 nm upon Zn(II)-binding. By exciting the probe at the isosbestic point, the observed emission intensities are a direct reflection of the quantum yield, which increases more than 2-fold from 0.32 to 0.71 upon Zn(II)-coordination (Figure 2B). Overall, the Zn(II)-induced fluorescence changes are well suited for emission-ratiometric measurements. For example, the ratio of the integrated fluorescence intensities between 510 and 570 nm and 440 and 495 nm increases from 0.7 to 2.6 upon saturation with Zn(II), corresponding to a large dynamic range R_{max}/R_{min} of 3.7.

Analogous to the UV−vis spectral properties, the two-photon absorption (2PA) cross section revealed a red-shifted maximum, which increased from 720 to 740 nm upon Zn(II)-coordination (Figure 2C). Consistent with greater excited-state polarization,[32] the 2PA cross section of the Zn(II)-bound form is significantly increased compared to the free form (Figure 2C). Nevertheless, in the range between 710 and 740 nm the probe offers balanced

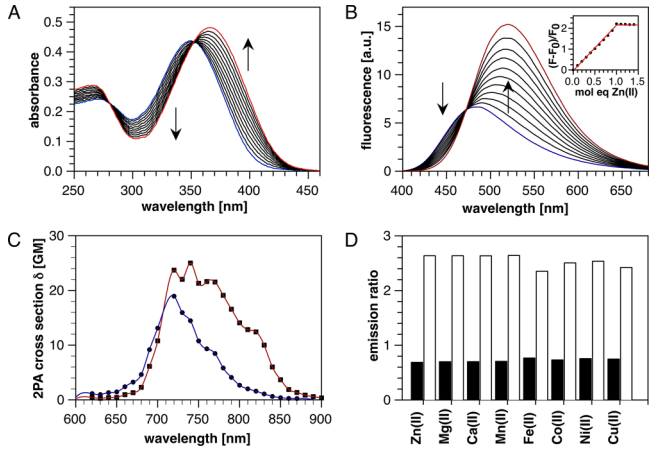

Figure 2. Spectral characteristics of chromis-1 acid (**1b**, 5 μM) in response to divalent metal cations in aqueous buffer (pH 7.0, 10 mM PIPES, 0.1 M KCl, 25 °C). (A) UV−vis absorption spectral changes upon saturation with Zn(II). (B) Fluorescence emission response upon saturation with Zn(II) (excitation at 358 nm). Inset: Fluorescence intensity at 520 nm as a function of molar equivalents of Zn(II). (C) Two-photon absorption cross section of the free (blue trace) and Zn(II)-bound (red trace) form of **1b**. (D) Emission-ratiometric response toward selected divalent metal cations at 80% fractional saturation in absence (black bars) or presence (white bars) of Zn(II). The emission ratio was calculated based on the integrated fluorescence intensity between 510 and 570 nm and 440 and 495 nm. Excitation: 358 nm.

Table 1. One and Two-Photon Photophysical Properties of Chromis-1 Ester (1a) and Acid (1b) in Aqueous Buffer at pH 7.0[a]

	1a[b,c]	[**1a**-Zn(II)][b]	**1b**[c]	[**1b**-Zn(II)]
abs λ_{max} (nm)[d]	351	378	349	366
$\varepsilon(10^4\ M^{-1}\ cm^{-1})$[e]	2.20	2.86	2.05	2.41
2PA λ_{max} (nm)[f]	n.d.	n.d.	720	740
δ_{max} (GM)[g]	n.d.	n.d.	19	25
em λ_{max} (nm)[h]	438	495	483	520
Φ_F[i]	0.26	0.56	0.32	0.71

[a]10 mM PIPES, 0.1 M KCl, 25 °C. [b]Buffer supplemented with 100 μM liposomes (4:1 DMPC:DMPG). [c]Supplemented with 20 μM EDTA to sequester adventitious Zn(II). [d]Lowest-energy band of the one-photon absorption spectrum. [e]Molar extinction coefficient at λ_{max}. [f]Maximum two-photon absorption. [g]Two-photon absorption cross section. [h]Maximum fluorescence emission. [i]Fluorescence quantum yield, referenced to quinine sulfate (Φ_F = 0.55).[23]

cross sections, allowing for excitation of the free and Zn(II)-bound probe with similar efficiency.

In contrast to Zn(II), all other biologically relevant divalent metal ions showed either no change in the emission response or complete fluorescence quenching (Figure S1). As both the probe and its Zn(II)-complex are brightly fluorescent, the quenched emission does not contribute to the ratiometric readout, thus binding of these metal ions results only in a masking effect by competing for Zn(II)-coordination. For this reason, we evaluated the selectivity of the ratio-response in the presence of 0.8 mol equiv of the interfering metal ion (Figure 2D, black bars). Under these conditions, the emission ratio of the remaining free probe was unaffected by any of the quenching metal ions, while addition of Zn(II) still produced the emission ratio response of the probe-Zn(II) complex (Figure 2D, white bars) as observed in the molar ratio titration (Figure 2B).

DOI: 10.1021/acssensors.7b00887
ACS Sens. 2018, 3, 458−467

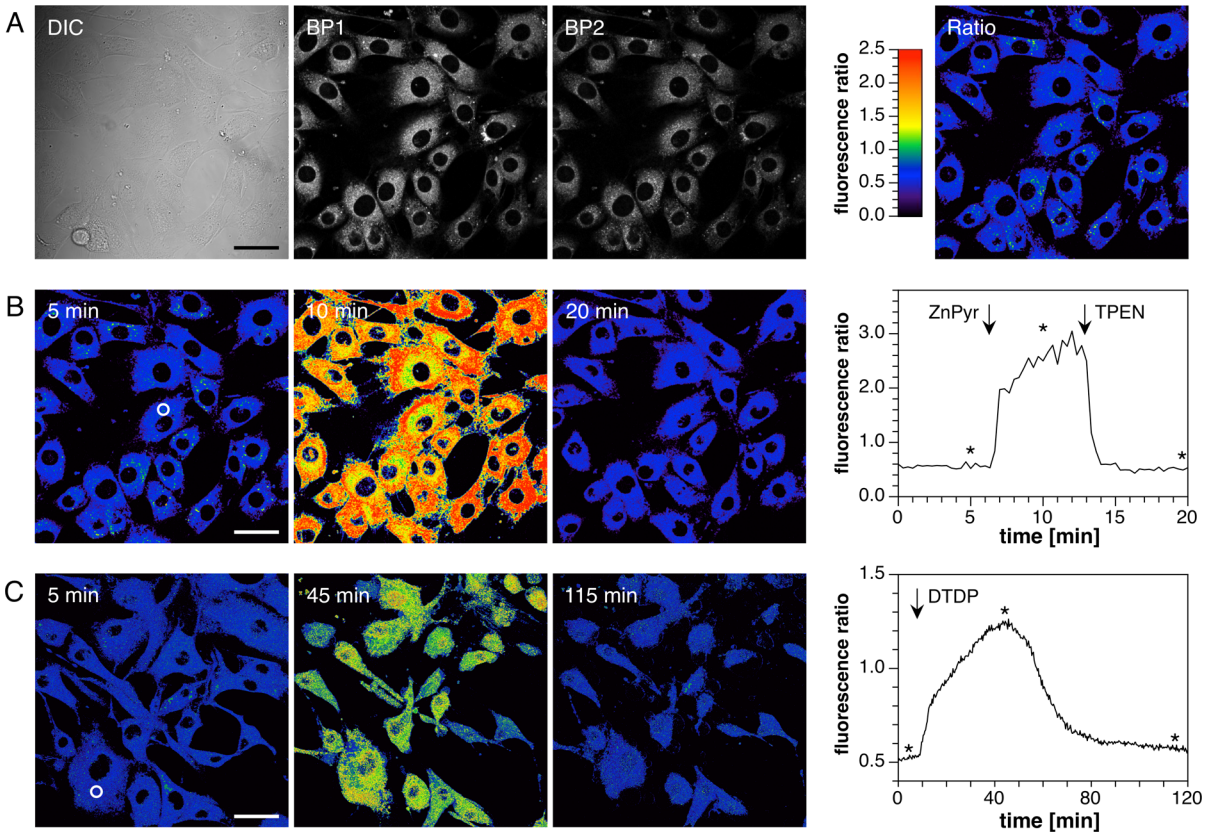

Figure 3. Ratiometric imaging of labile Zn(II) pools in live NIH 3T3 mouse fibroblasts with chromis-1 ester (**1a**) by TPEM (excitation at 720 nm). (A) Left: Phase contrast image (DIC) and fluorescence intensity images acquired with 425−462 nm (BP1) and 478−540 nm (BP2) bandpass filters, respectively. Right: Intensity ratio image with R = BP2/BP1. (B) Left: Ratio images (BP2/BP1) at selected time points prior and after addition of 50 μM $ZnSO_4$ and 5 μM pyrithione (ZnPyr). Further addition of 100 μM TPEN at 13 min resulted in a reversal of the intensity ratio (shown at 20 min). Right: Time course of the average intensity ratio change for the ROI indicated with a white circle in the left panel. The asterisks indicate time points for the respective ratio images shown to the left. (C) Left: Ratio images prior (at 5 min) and after addition of 100 μM DTDP (at 45 min). This treatment resulted first in a ratio increase peaking around 40 min followed by a gradual decrease back to the initial level (shown at 115 min). Right: Time course of the average intensity ratio change for the ROI indicated with a white circle. The asterisks indicate time marks for the respective ratio images to the left. Scale bars: 40 μm.

Binding Affinity. The linear emission increase together with sharp saturation at the equivalence point for the molar ratio titration shown in Figure 2B indicates tight Zn(II) binding with near unity fractional saturation throughout the entire titration range. Because the determination of reliable stability constants demands conditions where complex formation is incomplete, ideally within a 10−90% fractional saturation window,[33] we performed spectrophotometric titrations in the presence of EGTA as a competing ligand with matching affinity (apparent K_d = 4.0 nM at pH 7.0, calculated from published pK_a's and logβ values).[34] Regardless of whether the preformed Zn(II)-complex of chromis-1 acid **1b** was titrated with EGTA, or whether Zn(II) was added to a mixture of the probe and EGTA, least-squares fitting of the spectrophotometric data yielded a uniform apparent stability constant of log$K$ = 10.31 ± 0.13 at pH 7.0 and 0.1 M KCl ionic background (25 °C), corresponding to an apparent dissociation constant of 49 ± 13 pM (Figure S2). To gauge the effect of pH changes on the Zn(II) affinity, we also determined the protonation constants of chromis-1 acid **1b** through combined potentiometric and spectrophotometric titrations (Figure S5). Concluding from the derived experimental pK_a values of 5.5, 3.5, and 1.2, chromis-1 acid is almost exclusively present as the fully deprotonated dianionic species at neutral pH, and thus the apparent stability constant is not strongly affected by variations in cellular pH between 6 and 8. For example, the apparent Zn(II) affinity decreases only from log$K$ of 10.3 to 10.2 upon acidification from pH 8 to 6.

Because the anionic dicarboxylate salt **1b** is not membrane permeable, cellular imaging studies were performed with diester **1a** which is readily internalized and partitions within intracellular membranes (vide infra). To determine the apparent Zn(II) stability constant of **1a** under conditions that mimic the cellular environment, fluorimetric titrations were carried out in the presence of liposomes as model membranes, composed of a 4:1 ratio of zwitterionic dimyristoyl phosphatidylcholine (DMPC) and anionic dimyristoyl phosphatidylglycerol (DMPG). Upon dilution from a DMSO stock solution into pH 7.0 buffer containing 100 μM liposomes and 1.0 mM EGTA as competing ligand, diester **1a** was titrated up to a total concentration of 1 mM Zn(II). Nonlinear least-squares fitting of the fluorescence titration data over the entire spectral range yielded an average apparent log$K$ of 8.62 ± 0.07, corresponding to a K_d of 2.4 ± 0.4 nM (Figure S3). Consistent with a stronger electron withdrawing character of the neutral ester groups in **1a** compared to the anionic carboxylate substituents in **1b**, chromis-1 ester exhibits a Zn(II) affinity that is nearly 2 orders of magnitude lower. For the same reason, the ester form is also expected to exhibit lower protonation constants, thus further attenuating the effect of pH changes on the apparent Zn(II) affinity.

DOI: 10.1021/acssensors.7b00887
ACS Sens. 2018, 3, 458−467

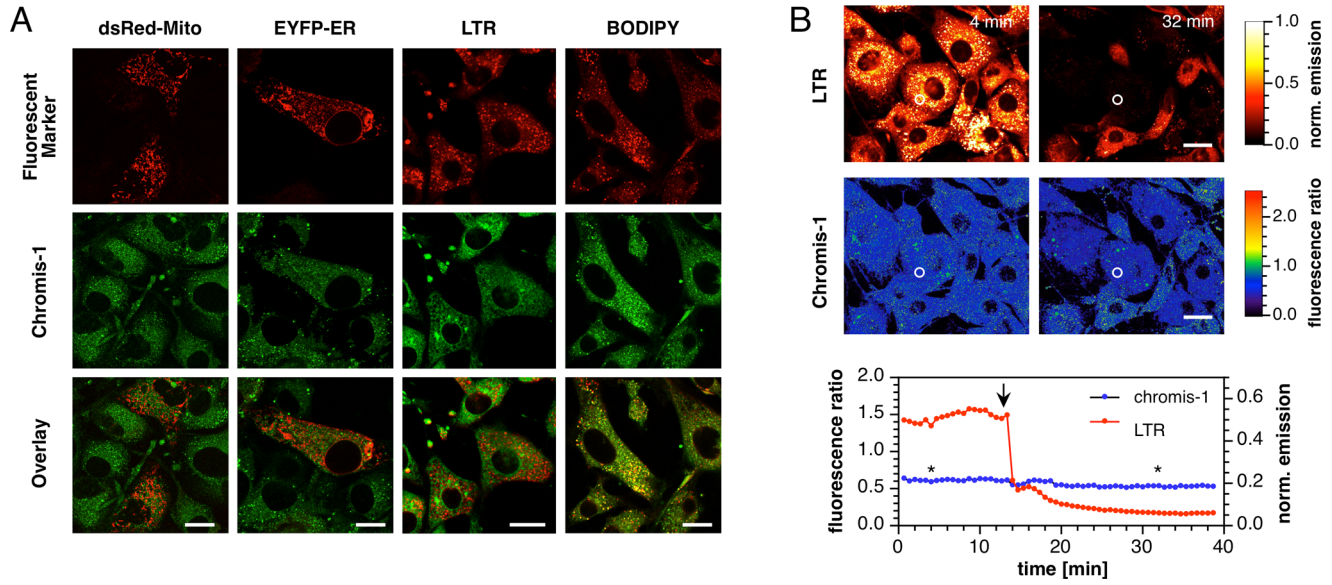

Figure 4. (A) Colocalization analysis of chromis-1 ester (**1a**) in NIH 3T3 mouse fibroblasts using selected cellular markers. Top row: Fluorescence micrograph of cells that express either dsRed-mito (first column, λ_{ex} = 561 nm, λ_{em} 570−700 nm) or EYFP-ER (second column, λ_{ex} = 514 nm, λ_{em} 525−675 nm) as mitochondrial or ER markers, respectively, or that are costained with LysoTracker Red (third column, λ_{ex} = 514 nm, λ_{em} 525−675 nm) or the lipid droplet marker BODIPY 493/503 (4th column, λ_{ex} = 488 nm, λ_{em} 525−675 nm). Center row: Two-photon fluorescence micrograph of the same cells costained with chromis-1 ester (λ_{ex} = 720 nm, λ_{em} 400−498 nm). Bottom row: Red-green false-color overlay images revealing spatial overlap between chromis-1 ester and the respective fluorescent cellular markers in yellow hues. (B) Emission ratiometric response of chromis-1 toward intracellular pH changes. Top panel: Live NIH 3T3 cells were coincubated with LysoTracker Red (LTR, 50 nM) and chromis-1 ester (2 μM) and fluorescence images were acquired simultaneously to assess changes in LTR fluorescence (top row, λ_{ex} = 514 nm, λ_{em} 525−675 nm) and chromis-1 emission ratio (λ_{ex} = 720 nm, ratio = BP2/BP1 BP1 = 425−462 nm, BP2 = 478−540 nm band-pass emission filters) upon addition of bafilomycin A_1 (900 nM) at 14 min. Bottom: Plot for the time-dependent changes of the average emission intensity of LTR (right scale, red trace) and intensity ratio of chromis-1 fluorescence (left scale, blue trace) for the ROI indicated with a white circle. The asterisk marks the time points for above micrographs, and the arrow shows the time point of bafilomycin A_1 addition. Scale bars: 20 μm.

Ratiometric Imaging of Cellular Zinc. To evaluate the Zn(II)-dependent ratiometric response of chromis-1 within the chemical complexity of a live cell, we performed a series of perfusion experiments with NIH 3T3 mouse fibroblasts as a model system (Figure 3). Live adherent cells were incubated with 10 μM chromis-1 ester **1a** in serum-free medium for 15 min at 37 °C and imaged by two-photon excitation at 720 nm using a Zeiss LSM 710 Confocal/NLO microscope. Fluorescence emission was collected with a polychromatic detector between 425 and 462 nm and 478 and 540 nm, and the corresponding ratio-images were derived based on the integrated photon counts on a pixel-per-pixel basis (Figure 3A, right). As evident from the intensity images (Figure 3A, middle), chromis-1 ester readily entered cells to yield bright fluorescence throughout the cytoplasm but was excluded from cell nuclei. Although the fluorescence intensity distribution appears uneven, including distinct punctate localizations, the corresponding ratio-image indicates a rather even fractional saturation with an average ratio R of 0.60 ± 0.16. Upon exposure to a mixture of $ZnSO_4$ and pyrithione, a membrane-permeable ionophore for Zn(II),[35] the intensity ratio rapidly increased by more than 4-fold to R = 2.53 ± 0.56, indicating saturation of the probe with Zn(II) (Figure 3B). Addition of the membrane-permeant high-affinity chelator TPEN (*N*,*N*,*N*′,*N*′-tetrakis(2-pyridylmethyl)ethylenediamine, apparent K_d = 9.3 fM at pH 7.0)[34] elicited a ratio response toward a slightly lower R value of 0.54 ± 0.13 compared to the initial conditions. A similar R value of 0.52 ± 0.14 was obtained when TPEN was directly added to cells grown in basal medium without prior exposure to the Zn(II)-pyrithione mixture (Figure S7). A plot of the intensity ratio vs time revealed rapid dynamics for Zn(II)-binding and release, both of which occurred within a few seconds (Figure 3B, right). Using the ratios in the presence of TPEN and Zn(II)-pyrithione as the limiting R_{min} and R_{max} values, respectively, 3T3 cells grown under basal conditions display a fractional saturation around 3−6%. Based on the measured K_d of 2.4 nM of chromis-1 ester, we estimated an average buffered Zn(II) concentration in the range of 50−100 pM. This value agrees well with previous reports on the buffered concentration of cytosolic free Zn(II), ranging between 0.1 and 1 nM in a broad range of cell types.[36−38] Although chromis-1 ester could be subject to hydrolysis by nonspecific esterases, the subcellular distribution with a pronounced association with neutral lipids (vide infra) and nuclear exclusion indicates that the probe remains intact in its charge-neutral ester form.

To explore whether chromis-1 can be utilized to follow dynamic fluctuations of endogenous Zn(II) pools, cells were exposed to 2,2′-dithiodipyridine (DTDP), an oxidizing agent that is expected to induce dissociation of Zn(II) ions from cellular sulfhydryl binding sites as present, for example, in metallothionein.[39] Consistent with the initial perfusion experiment (Figure 3B, left), cells grown under basal conditions and treated with chromis-1 ester produced similarly low intensity ratios around 0.5 (Figure 3C, left), which gradually increased upon addition of 100 μM DTDP, reaching a maximum after 40 min with an average around 1.3 (Figure 3C, middle). The dramatic ratio increase was followed by a gradual decrease without addition of an exogenous reagent, thus indicating re-equilibration of cytoplasmic Zn(II) levels back to basal conditions with an intensity ratio around 0.5.

DOI: 10.1021/acssensors.7b00887
ACS Sens. 2018, 3, 458−467

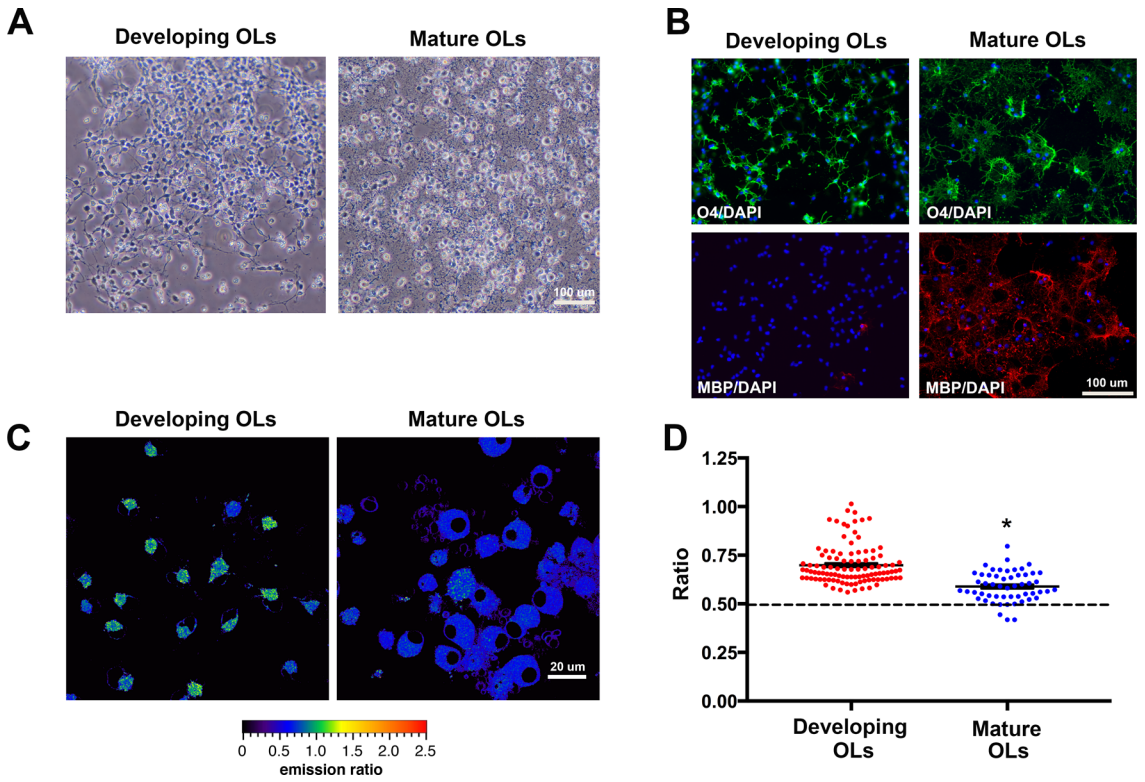

Figure 5. (A) Phase contrast microscopy images of developing oligodendrocytes at DIV9 and mature oligodendrocytes at DIV16. (B) Immunocytochemistry for O4 antigen (O4, green), myelin basic protein (MBP, red) and DAPI (blue) in developing and mature oligodendrocytes. (C) Representative chromis-1 ratio images for developing and mature oligodendrocytes at DIV9 and DIV16 respectively. (D) Scatterplot for chromis-1 ratios of individual developing (red) and mature (blue) oligodendrocytes. Mean ± SEM shown with black solid lines and indicated a decrease in ratio in mature oligodendrocytes compared to developing oligodendrocytes. * $P < 0.0001$ (t test developing vs mature oligodendrocytes). Broken line indicates average ratio after application of TPEN.

Subcellular Localization of Chromis-1. The nonuniform staining pattern of chromis-1 ester in 3T3 cells suggests specific localization to subcellular structures. To elucidate potential associations with cellular organelles, we utilized selective fluorescent protein markers and live cell stains to perform colocalization studies. To this end, 3T3 cells were either transfected with plasmids encoding for mitochondrial (pDsRed2-mito) or endoplasmic reticulum (pEYFP-ER) organelle markers or costained with LysoTracker Red (LTR) or BODIPY 493/50 for visualizing acidic compartments or neutral lipids, respectively.[40] As shown in Figure 4A, the fluorescence staining pattern of chromis-1 ester (green) revealed minimal spatial correlation with the subcellular distribution of LysoTracker Red or the mitochondrial and ER marker proteins (red); however, significant overlap with the BODIPY lipid marker was observed (last column). Consistent with its lipophilic properties, chromis-1 ester **1a** preferentially associates with intracellular membranes and other lipid-rich regions.

Sensitivity toward Cellular pH Fluctuations. To test the ratiometric response of chromis-1 ester toward interference from changes in cellular pH, live fibroblasts cells were exposed to 900 nM bafilomycin A_1, a selective inhibitor of vacuolar-type H^+-ATPases.[41,42] In order to dynamically track the effect of bafilomycin A_1, cells were incubated with LysoTracker Red in addition to chromis-1 ester. Functionalized with a weak base, LysoTracker Red acts as an acidotropic dye that is rendered membrane impermeable upon protonation and thus selectively accumulates within acidic compartments such as lysosomes. As shown in Figure 4B, the fluorescence intensity of LysoTracker Red was immediately attenuated upon addition of bafilomycin A_1, thus indicating rapid pH-equilibration of the stained acidic compartments and surrounding cytosol. In contrast, negligible changes were detected for the ratiometric response of chromis-1 ester. This result is consistent with in vitro studies using liposomes as model membranes, where only small changes of the fluorescence emission were observed upon acidification from pH 7 to pH 5 (Figure S4).

Probing Labile Zn(II) Pools in Developing Oligodendrocytes. Zinc is abundant in the central nervous system but tightly regulated, with the majority of Zn(II) bound to proteins or sequestered in intracellular organelles. At the same time, a fraction of total cellular Zn(II) is kinetically labile and has been increasingly recognized to play important signaling roles in the brain.[11] To test whether chromis-1 is suitable for visualizing alterations of this labile pool in a system relevant to zinc regulation within the central nervous system, we assessed differences in intracellular free zinc concentrations in oligodendrocytes at different stages of development. The development of oligodendrocytes occurs following a well-characterized lineage that can be identified using antibodies against cell surface antigens. Representative phase contrast images of developing and mature oligodendrocytes and fluorescence immunohistochemistry images obtained using the O4 antigen (O4) as a marker of developing oligodendrocytes, myelin basic protein (MBP) as a marker of mature oligodendrocytes, and DAPI as nuclear counter stain are shown in Figure 5A and B. As expected, there was virtually no MBP expression in developing oligodendrocytes, but robust expression in mature oligoden-

DOI: 10.1021/acssensors.7b00887
ACS Sens. 2018, 3, 458−467

drocytes. Similar cultures were used for all subsequent imaging experiments. Cells were loaded with chromis-1 ester (10 μM) in serum-free medium and then imaged within 60 min. Baseline intensity ratios were determined in both developing and mature oligodendrocytes. As shown in Figure 5C, the Zn(II)-saturation of chromis-1 was decreased in mature versus developing oligodendrocytes as judged from the different intensity ratios of 0.59 ± 0.01 (n = 54 cells from 3 different cultures) vs 0.70 ± 0.01 (n = 103 cells from 3 different cultures), respectively (p < 0.0001).

To determine the limiting emission intensity ratios R_{min} and R_{max}, we conducted experiments analogous to those with mouse fibroblast cells by applying either TPEN (100 μM) or Zn(II)-pyrithione (50 μM $ZnCl_2$ and 5 μM pyrithione), respectively. Addition of TPEN to the medium resulted in an immediate decrease of the emission ratio to 0.49 ± 0.008 in developing oligodendrocytes (n = 46 cells from 3 different cultures) and 0.51 ± 0.003 in mature oligodendrocytes (n = 28 cells from 3 different cultures). These values are in close agreement with R_{min} determined in mouse fibroblast cells and indicate a robust probe response regardless of cell type. Moreover, the reduction to a uniform R_{min} starting from different cell-type dependent baseline ratios is consistent with quantitative depletion of labile Zn(II) from the probe. Similarly, saturation of chromis-1 upon incubation with exogenous Zn(II)-pyrithione yielded an R_{max} value of 2.76 ± 0.03 in developing oligodendrocytes (n = 21 cells from 2 different cultures) and 2.47 ± 0.04 in mature oligodendrocytes (n = 31 cells from 3 different cultures), again closely mirroring the response observed in mouse fibroblast cells. Altogether, these experiments demonstrate a robust and reproducible emission-ratiometric response of chromis-1, regardless of the specific biological system. Based on the limiting R_{min} and R_{max} values, we calculated a fractional saturation of 8–9% in developing and 3.5–6.5% in mature oligodendrocytes, thus translating into estimated Zn(II)-levels of 135–152 pM and 65–95 pM, respectively.

The decrease in Zn(II) levels as oligodendrocytes mature may play a role in the differentiation of these cells. Several zinc-finger transcription factors have been identified that are critical for proper oligodendrocyte differentiation.[43−46] Modulation of intracellular zinc concentrations alters nuclear interactions of at least one of these transcription factors, Ying Yang-1,[47] highlighting a mechanism by which changes in intracellular zinc status may promote epigenetic modifications. A second mechanism by which intracellular free zinc concentrations may influence differentiation is by the regulation of enzyme function, as zinc acts as a cofactor for several hundred enzymes.[48] A classic example of this type of regulation is the calcium-calmodulin pathway where the activity of proteins is directly modulated by alterations in intracellular calcium concentrations, leading to well characterized signaling cascades.[49] Similar zinc signaling pathways are increasingly being identified. As a single example, the ERK signaling pathway is essential for oligodendrocyte differentiation[50] and the conversion from phosphorylated ERK to dephosphorylated ERK is directly regulated by intracellular zinc concentrations.[51] In addition, proliferating cells require higher zinc concentrations to promote DNA synthesis and regulate cell cycle progression.[12,52] The change in zinc status may reflect the transition from proliferating to differentiating phenotype. Finally, zinc ions also stabilize association of myelin basic protein with myelin membranes,[53] so the expression of MBP may contribute to the reduction in free cytosolic zinc.

CONCLUSIONS

Optimized for ratiometric two-photon excitation microscopy, the fluorescent probe chromis-1 features a balanced brightness and large emission shift upon saturation with Zn(II). By integrating the metal-binding site within the framework of a donor−acceptor substituted fluorophore platform, the emission shift was achieved without compromising the two-photon cross section. Because background noise is amplified in the ratio image compared to the raw signal of each channel, a balanced brightness between the free and Zn(II)-bound form as offered by chromis-1 is a critical prerequisite for robust quantitative ratiometric image analysis. Although a large R_{max}/R_{min} ratio might appear advantageous, the apparent increase in dynamic range would be offset by the increased noise due to the limited dynamic range of the detector system.

In situ measurements in three different cell systems established uniform R_{min} and R_{max} values from which we were able to estimate the corresponding levels of cytosolic Zn(II). As demonstrated with differentiating oligodendrocytes, ratiometric two-photon microscopy is especially well suited for visualizing subtle changes of physiologically relevant Zn(II) levels. While cytosolic Zn(II) in developing oligodendrocytes ranged between 135 and 152 pM, mature MBP cells revealed nearly 2-fold lower levels in the 65−95 pM range. These values reside well within the concentration window reported for cell systems that were analyzed based on genetically encoded ratiometric fluorescence probes. For example, the level of cytosolic Zn(II) was estimated to be 80 pM in HeLa cells,[36] 270 pM in HEK293 cells,[37] or 400 pM in INS-1 pancreatic β cells.[37] It is important to note that ratiometric image analysis informs only on the fractional saturation of the probe, not the actual buffered Zn(II) levels. The latter must be derived on the basis of independent probe-calibration procedures, which are typically carried out in vitro. Due to variations in calibration conditions, such as temperature, pH, or ionic background, and the discrepancies of reported protonation constants and Zn(II) affinities of the employed competitor ligands and metal ion buffers, the derived cellular Zn(II) levels should be considered as estimates. Nevertheless, ratiometric imaging represents a powerful approach to visualize relative changes in dynamic Zn(II)-availability as demonstrated across the oligodendrocyte lineage. With the ability to visualize physiologically relevant changes in mobile Zn(II) levels, chromis-1 is well poised to untangle specific molecular pathways that regulate zinc homeostasis and zinc signaling in a broad range of biological systems.

ASSOCIATED CONTENT

Supporting Information

The Supporting Information is available free of charge on the ACS Publications website at DOI: 10.1021/acssensors.7b00887.

Synthetic procedures, compound characterization, crystal structure data, details of the determination of Zn(II) stability constants, protonation constants, and ratiometric imaging data analysis (PDF)

Crystallographic data (CIF)

AUTHOR INFORMATION

Corresponding Authors

*E-mail: joe.perry@gatech.edu.

*E-mail: Paul.Rosenberg@childrens.harvard.edu.

*E-mail: fahrni@chemistry.gatech.edu.

DOI: 10.1021/acssensors.7b00887
ACS Sens. 2018, 3, 458−467

ORCID

Joseph W. Perry: 0000-0003-1101-7337

Christoph J. Fahrni: 0000-0003-3731-7434

Author Contributions

‡D.B. and C.M.E. contributed equally to this work.

Notes

The authors declare no competing financial interest.

■ ACKNOWLEDGMENTS

We thank Dr. John Bacsa, Emory X-ray Crystallography Facility for the X-ray structural analysis. We also acknowledge the use of the Rigaku SYNERGY diffractometer, supported by the National Science Foundation under grant CHE-1626172. Financial support from the National Science Foundation through grant CHE-1306943 (to CJF) and the National Institutes of Health through grants DK68096 and GM067169 (to CJF), HD018655 and EY024481 (to PAR), as well as NS070682 and NINDS NS079414 (to CME), is gratefully acknowledged. We also acknowledge financial support from the Baby Alex Foundation, National Multiple Sclerosis Foundation, The William Randolph Hearst Foundation, and Genise Goldenson Research Award (to CME).

■ REFERENCES

(1) Liu, Z.; He, W.; Guo, Z. Metal coordination in photoluminescent sensing. *Chem. Soc. Rev.* **2013**, *42* (4), 1568−600.

(2) Schießl, I. M.; Castrop, H. Deep insights: intravital imaging with two-photon microscopy. *Pflügers Arch.* **2016**, *468* (9), 1505−16.

(3) Yao, S.; Belfield, K. D. Two-photon fluorescent probes for bioimaging. *Eur. J. Org. Chem.* **2012**, *2012*, 3199−3217.

(4) Albota, M. A.; Xu, C.; Webb, W. W. Two-photon fluorescence excitation cross sections of biomolecular probes from 690 to 960 nm. *Appl. Opt.* **1998**, *37* (31), 7352−6.

(5) Sarkar, A. R.; Kang, D. E.; Kim, H. M.; Cho, B. R. Two-photon fluorescent probes for metal ions in live tissues. *Inorg. Chem.* **2014**, *53* (4), 1794−803.

(6) Demchenko, A. P. The concept of *θ*-ratiometry in fluorescence sensing and imaging. *J. Fluoresc.* **2010**, *20* (5), 1099−1128.

(7) Yellen, G.; Mongeon, R. Quantitative two-photon imaging of fluorescent biosensors. *Curr. Opin. Chem. Biol.* **2015**, *27*, 24−30.

(8) Kim, H. M.; Cho, B. R. Small-molecule two-photon probes for bioimaging applications. *Chem. Rev.* **2015**, *115* (11), 5014−55.

(9) Sumalekshmy, S.; Henary, M. M.; Siegel, N.; Lawson, P. V.; Wu, Y.; Schmidt, K.; Brédas, J. L.; Perry, J. W.; Fahrni, C. J. Design of emission ratiometric metal-ion sensors with enhanced two-photon cross section and brightness. *J. Am. Chem. Soc.* **2007**, *129* (39), 11888−11889.

(10) Simons, M.; Nave, K. A. Oligodendrocytes: myelination and axonal support. *Cold Spring Harbor Perspect. Biol.* **2016**, *8* (1), a020479.

(11) Sensi, S. L.; Paoletti, P.; Bush, A. I.; Sekler, I. Zinc in the physiology and pathology of the CNS. *Nat. Rev. Neurosci.* **2009**, *10* (11), 780−91.

(12) McRae, R.; Lai, B.; Fahrni, C. J. Subcellular redistribution and mitotic inheritance of transition metals in proliferating mouse fibroblast cells. *Metallomics* **2013**, *5* (1), 52−61.

(13) Koh, J. Y.; Suh, S. W.; Gwag, B. J.; He, Y. Y.; Hsu, C. Y.; Choi, D. W. The role of zinc in selective neuronal death after transient global cerebral ischemia. *Science* **1996**, *272* (5264), 1013−6.

(14) Li, Y.; Andereggen, L.; Yuki, K.; Omura, K.; Yin, Y.; Gilbert, H. Y.; Erdogan, B.; Asdourian, M. S.; Shrock, C.; de Lima, S.; Apfel, U. P.; Zhuo, Y.; Hershfinkel, M.; Lippard, S. J.; Rosenberg, P. A.; Benowitz, L. Mobile zinc increases rapidly in the retina after optic nerve injury and regulates ganglion cell survival and optic nerve regeneration. *Proc. Natl. Acad. Sci. U. S. A.* **2017**, *114* (2), E209−E218.

(15) Mato, S.; Sánchez-Gómez, M. V.; Bernal-Chico, A.; Matute, C. Cytosolic zinc accumulation contributes to excitotoxic oligodendroglial death. *Glia* **2013**, *61* (5), 750−64.

(16) Zhang, Y.; Wang, H.; Li, J.; Dong, L.; Xu, P.; Chen, W.; Neve, R. L.; Volpe, J. J.; Rosenberg, P. A. Intracellular zinc release and ERK phosphorylation are required upstream of 12-lipoxygenase activation in peroxynitrite toxicity to mature rat oligodendrocytes. *J. Biol. Chem.* **2006**, *281* (14), 9460−70.

(17) Domercq, M.; Mato, S.; Soria, F. N.; Sánchez-Gómez, M. V.; Alberdi, E.; Matute, C. Zn^{2+}-induced ERK activation mediates PARP-1-dependent ischemic-reoxygenation damage to oligodendrocytes. *Glia* **2013**, *61* (3), 383−93.

(18) Frederickson, C. J.; Koh, J. Y.; Bush, A. I. The neurobiology of zinc in health and disease. *Nat. Rev. Neurosci.* **2005**, *6* (6), 449−62.

(19) Sheldrick, G. M. SHELXT - Integrated space-group and crystal-structure determination. *Acta Crystallogr., Sect. A: Found. Adv.* **2015**, *71*, 3−8.

(20) Dolomanov, O. V.; Bourhis, L. J.; Gildea, R. J.; Howard, J. A. K.; Puschmann, H. OLEX2: a complete structure solution, refinement and analysis program. *J. Appl. Crystallogr.* **2009**, *42*, 339−341.

(21) Sheldrick, G. M. Crystal structure refinement with SHELXL. *Acta Crystallogr., Sect. C: Struct. Chem.* **2015**, *71*, 3−8.

(22) Morgan, M. T.; McCallum, A. M.; Fahrni, C. J. Rational design of a water-soluble, lipid-compatible fluorescent probe for Cu(I) with sub-part-per-trillion sensitivity. *Chem. Sci.* **2016**, *7* (2), 1468−1473.

(23) Brouwer, A. M. Standards for photoluminescence quantum yield measurements in solution (IUPAC Technical Report). *Pure Appl. Chem.* **2011**, *83* (12), 2213−2228.

(24) Binstead, R. A.; Zuberbühler, A. D. *SPECFIT Global Analysis System*; Spectrum Software Associates, Marlborough MA 01752, 2001.

(25) Gans, P.; O'Sullivan, B. GLEE, a new computer program for glass electrode calibration. *Talanta* **2000**, *51* (1), 33−37.

(26) DeSilva, T. M.; Kabakov, A. Y.; Goldhoff, P. E.; Volpe, J. J.; Rosenberg, P. A. Regulation of glutamate transport in developing rat oligodendrocytes. *J. Neurosci.* **2009**, *29* (24), 7898−908.

(27) Schneider, C. A.; Rasband, W. S.; Eliceiri, K. W. NIH Image to ImageJ: 25 years of image analysis. *Nat. Methods* **2012**, *9* (7), 671−5.

(28) Kojima, T.; Hayashi, K. I.; Iizuka, S. Y.; Tani, F.; Naruta, Y.; Kawano, M.; Ohashi, Y.; Hirai, Y.; Ohkubold, K.; Matsuda, Y.; Fukuzumi, S. Synthesis and characterization of mononuclear ruthenium-(III) pyridylamine complexes and mechanistic insights into their catalytic alkane functionalization with *m*-chloroperbenzoic acid. *Chem. - Eur. J.* **2007**, *13* (29), 8212−8222.

(29) Allen, C. S.; Chuang, C.-L.; Cornebise, M.; Canary, J. W. Electrospray mass spectrometry and X-ray crystallography studies of divalent metal ion complexes of tris(2-pyridylmethyl) amine. *Inorg. Chim. Acta* **1995**, *239* (1), 29−37.

(30) Adams, H.; Bailey, N. A.; Fenton, D. E.; He, Q.-Y. Mononuclear zinc(II), homodinuclear zinc(II) and heterodinuclear zinc(II)-copper-(II) complexes derived from tris[(2-pyridyl)methyl] amine. *J. Chem. Soc., Dalton Trans.* **1997**, No. 9, 1533−1540.

(31) Duboc, C.; Phoeung, T.; Jouvenot, D.; Blackman, A. G.; McClintock, L. F.; Pécaut, J.; Collomb, M.-N.; Deronzier, A. High-field EPR investigation of a series of mononuclear Mn(II) complexes doped into Zn(II) hosts. *Polyhedron* **2007**, *26* (18), 5243−5249.

(32) Sumalekshmy, S.; Fahrni, C. J. Metal-ion-responsive fluorescent probes for two-photon excitation microscopy. *Chem. Mater.* **2011**, *23*, 483.

(33) Hansen, L. D.; Fellingham, G. W.; Russell, D. J. Simultaneous determination of equilibrium constants and enthalpy changes by titration calorimetry: Methods, instruments, and uncertainties. *Anal. Biochem.* **2011**, *409* (2), 220−9.

(34) Martell, A. E.; Smith, R. M.; Motekaitis, R. J. *NIST standard reference database 46 version 8.0: NIST critically selected stability constants of metal complexes*; National Institute of Standards and Technology, 2004.

(35) Forbes, I. J.; Zalewski, P. D.; Hurst, N. P.; Giannakis, C.; Whitehouse, M. W. Zinc increases phorbol ester receptors in intact B-cells, neutrophil polymorphs and platelets. *FEBS Lett.* **1989**, *247* (2), 445−7.

(36) Qin, Y.; Dittmer, P. J.; Park, J. G.; Jansen, K. B.; Palmer, A. E. Measuring steady-state and dynamic endoplasmic reticulum and Golgi

DOI: 10.1021/acssensors.7b00887
ACS Sens. 2018, 3, 458−467

Zn^{2+} with genetically encoded sensors. *Proc. Natl. Acad. Sci. U. S. A.* **2011**, *108* (18), 7351−6.
(37) Vinkenborg, J. L.; Nicolson, T. J.; Bellomo, E. A.; Koay, M. S.; Rutter, G. A.; Merkx, M. Genetically encoded FRET sensors to monitor intracellular Zn^{2+} homeostasis. *Nat. Methods* **2009**, *6* (10), 737−740.
(38) Hessels, A. M.; Merkx, M. Genetically-encoded FRET-based sensors for monitoring Zn^{2+} in living cells. *Metallomics* **2015**, *7* (2), 258−266.
(39) Aizenman, E.; Stout, A. K.; Hartnett, K. A.; Dineley, K. E.; McLaughlin, B.; Reynolds, I. J. Induction of neuronal apoptosis by thiol oxidation: Putative role of intracellular zinc release. *J. Neurochem.* **2000**, *75* (5), 1878−1888.
(40) Gocze, P. M.; Freeman, D. A. Factors underlying the variability of lipid droplet fluorescence in MA-10 Leydig tumor cells. *Cytometry* **1994**, *17* (2), 151−158.
(41) Yoshimori, T.; Yamamoto, A.; Moriyama, Y.; Futai, M.; Tashiro, Y. Bafilomycin A_1, a specific inhibitor of vacuolar-type H^+-ATPase, inhibits acidification and protein degradation in lysosomes of cultured cells. *J. Biol. Chem.* **1991**, *266* (26), 17707−12.
(42) Umata, T.; Moriyama, Y.; Futai, M.; Mekada, E. The cytotoxic action of diphtheria toxin and its degradation in intact Vero cells are inhibited by bafilomycin A_1, a specific inhibitor of vacuolar-type H^+-ATPase. *J. Biol. Chem.* **1990**, *265* (35), 21940−5.
(43) Zolova, O. E.; Wight, P. A. YY1 negatively regulates mouse myelin proteolipid protein (Plp1) gene expression in oligodendroglial cells. *ASN Neuro* **2011**, *3* (4), No. e00067.
(44) Soundarapandian, M. M.; Selvaraj, V.; Lo, U. G.; Golub, M. S.; Feldman, D. H.; Pleasure, D. E.; Deng, W. Zfp488 promotes oligodendrocyte differentiation of neural progenitor cells in adult mice after demyelination. *Sci. Rep.* **2011**, *1*, 2.
(45) Wang, S. Z.; Dulin, J.; Wu, H.; Hurlock, E.; Lee, S. E.; Jansson, K.; Lu, Q. R. An oligodendrocyte-specific zinc-finger transcription regulator cooperates with Olig2 to promote oligodendrocyte differentiation. *Development* **2006**, *133* (17), 3389−98.
(46) Vana, A. C.; Lucchinetti, C. F.; Le, T. Q.; Armstrong, R. C. Myelin transcription factor 1 (Myt1) expression in demyelinated lesions of rodent and human CNS. *Glia* **2007**, *55* (7), 687−97.
(47) Krapivinsky, G.; Krapivinsky, L.; Manasian, Y.; Clapham, D. E. The TRPM7 chanzyme is cleaved to release a chromatin-modifying kinase. *Cell* **2014**, *157* (5), 1061−72.
(48) Kochańczyk, T.; Drozd, A.; Krężel, A. Relationship between the architecture of zinc coordination and zinc binding affinity in proteins−insights into zinc regulation. *Metallomics* **2015**, *7* (2), 244−57.
(49) Carafoli, E.; Krebs, J. Why Calcium? How Calcium Became the Best Communicator. *J. Biol. Chem.* **2016**, *291* (40), 20849−20857.
(50) Ishii, A.; Furusho, M.; Bansal, R. Sustained activation of ERK1/2 MAPK in oligodendrocytes and schwann cells enhances myelin growth and stimulates oligodendrocyte progenitor expansion. *J. Neurosci.* **2013**, *33* (1), 175−86.
(51) Nuttall, J. R.; Oteiza, P. I. Zinc and the ERK kinases in the developing brain. *Neurotoxic. Res.* **2012**, *21* (1), 128−41.
(52) Li, Y.; Maret, W. Transient fluctuations of intracellular zinc ions in cell proliferation. *Exp. Cell Res.* **2009**, *315* (14), 2463−70.
(53) Earl, C.; Chantry, A.; Mohammad, N.; Glynn, P. Zinc ions stabilise the association of basic protein with brain myelin membranes. *J. Neurochem.* **1988**, *51* (3), 718−24.

DOI: 10.1021/acssensors.7b00887
ACS Sens. 2018, 3, 458−467